Rare-earth/transition-metal magnets at finite temperature: Self-interaction-corrected relativistic density functional theory in the disordered local moment picture

Christopher E. Patrick[*] and Julie B. Staunton

Department of Physics, University of Warwick, Coventry CV4 7AL, United Kingdom

Atomic-scale computational modeling of technologically relevant permanent magnetic materials faces two key challenges. First, a material's magnetic properties depend sensitively on temperature, so the calculations must account for thermally induced magnetic disorder. Second, the most widely used permanent magnets are based on rare-earth elements, whose highly localized $4f$ electrons are poorly described by standard electronic structure methods. Here, we take two established theories, the disordered local moment picture of thermally induced magnetic disorder and self-interaction-corrected density functional theory, and devise a computational framework to overcome these challenges. Using this approach, we calculate magnetic moments and Curie temperatures of the rare-earth cobalt (RECo$_5$) family for RE = Y-Lu. The calculations correctly reproduce the experimentally measured trends across the series and confirm that, apart from the hypothetical compound EuCo$_5$, SmCo$_5$ has the strongest magnetic properties at high temperature. An order-parameter analysis demonstrates that varying the RE has a surprisingly strong effect on the Co-Co magnetic interactions determining the Curie temperature, even when the lattice parameters are kept fixed. We propose the origin of this behavior is a small contribution to the density from f-character electrons located close to the Fermi level.

I. INTRODUCTION

In solids, the 15 lanthanides (atomic numbers 57–71) usually exist in a 3+ state, with three electrons (two of s and one of d character) donated to the valence band. Grouping the lanthanides with Y and Sc, which behave in the same way, forms the group of elements known as the "rare earths" (REs) [1]. The chemical variation within the REs originates from their strongly localized $4f$ spin-up and -down subshells, which vary from being totally empty (Sc/Y/La, $4f^0$) to totally filled (Lu, $4f^{14}$). Lying at the center of the lanthanide block, Gd ($4f^7$) has one completely filled and one completely empty spin subshell, and marks the boundary between the "light" (Sc-Eu) and the "heavy" REs (Gd-Lu). Notable anomalous lanthanides include Ce, whose valence varies due to the relative ease that its single $4f$ electron can delocalize; Pm, which is radioactively unstable; and Eu and Yb which, rather than having a single hole in a spin subshell associated with the 3+ state, usually prefer to capture an additional $4f$ electron and adopt a 2+ state [1,2].

Aside from their uses in, e.g., catalysts, batteries, and energy-efficient lighting [3], the excellent magnetic properties of Sm-Co [4] and Nd-Fe-B [5,6] compounds have led to REs becoming critical to many industries as components in high-performance permanent magnets [7]. The key principle underlying such magnets is that while elemental transition metals (TMs) like Fe and Co remain strongly magnetic up to very high temperatures ($\sim$1000 K), they are relatively easy to demagnetize with external fields [8]. Alloying the elemental TMs with the REs largely retains their good high-temperature properties while simultaneously providing a massive increase in the coercivity (resistance to demagnetization) [8].

The principal microscopic mechanism driving this increased coercivity is the electrostatic interaction of the localized RE-$4f$ electrons with their environment (the crystal field) [9]. The magnetic moment associated with the RE-$4f$ electrons gains a strong directional preference, i.e., magnetocrystalline anisotropy, which anchors the TM magnetism along the same axis through the RE-TM exchange interaction. The benefits of this alloying approach can be seen in SmCo$_5$, whose Curie temperature (T_C) of 1020 K is comparable to pure Co (1360 K) [8,10] but whose magnetocrystalline anisotropy energy density is 20 times larger [11]. Indeed, over 50 years since its discovery the high-temperature properties of SmCo$_5$ remain hard to beat [7].

This simple picture, that the RE provides the coercivity and the TM provides the large magnetization and T_C, is an oversimplification since it neglects the contribution to the magnetization from the REs themselves. A more coherent picture of RE-TM intermetallics [9] models the RE as an array of isolated 3+ ions interacting with the crystal field and an effective magnetic field originating from the RE-TM exchange interaction. Diagonalization of the crystal-field Hamiltonian gives the RE contribution to the magnetization and anisotropy. The TM contribution is deduced empirically from RE-TM compounds with a nonmagnetic RE, like Y [12].

The crystal-field picture does an excellent job of explaining the temperature dependence of magnetic quantities which are heavily RE dependent, such as the low-temperature anisotropy and magnetization [9,12]. However, the phenomenological description of the TM limits the predictive power of the theory, especially with regard to T_C. Since a material rapidly loses its magnetic properties at temperatures in the vicinity of its Curie temperature, having a high T_C is very useful for practical permanent magnets. It is known experimentally

---
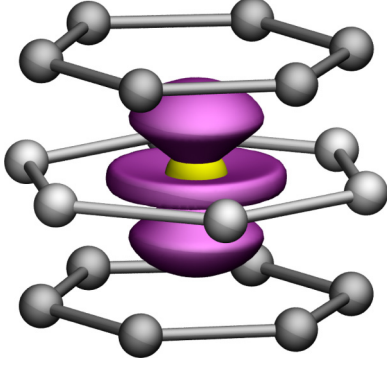
*c.patrick.1@warwick.ac.uk

FIG. 1. Schematic of the $RECo_5$ crystal structure, showing the RE (yellow) and Co sites (gray). The $2c$ sites (referred to as Co_I in the text) are in plane with the RE, and the $3g$ sites (Co_{II}) lie above and below. An isosurface plot representing the Sm-$4f$ charge density, obtained as the sum of the squared spherical harmonics with $l = 3$, $m = 3, 2, \ldots, -1$ is also shown.

that T_C is RE dependent: referring to the experimental review of Ref. [10], $SmCo_5$ has the highest T_C of the compounds that form stoichiometrically as $RECo_5$ (1020 K), slightly higher than $GdCo_5$ (1014 K). Meanwhile, for the RE_2Co_7 and RE_2Co_{17} series of magnets it is RE = Gd which has the highest T_C (771/1218 K) with RE = Sm lower (713/1195 K). The fact that Gd has the largest spin moment of the REs might suggest some correlation of this quantity with T_C, but the RE_2Co_7 series provides the counterexamples of RE = Dy and Ho, whose nominal spin moments are larger than Sm but whose T_C is smaller (640 and 647 K) [10]. Magnetostructural effects could also play a role, with the RE modifying the lattice constants and thus the magnetic interactions [13]. However, it is by no means clear how these and other effects might combine to influence T_C.

A predictive, first-principles theory of the T_C of RE-TM magnets could provide insight into the physical processes governing the high-temperature performance of these magnets, and suggest strategies for further optimization. However, such a theory is currently missing. Density functional theory (DFT) [14] provides a practical framework to perform first-principles studies of RE-TM magnets, but is faced with the challenge of describing with sufficient accuracy (i) the finite-temperature disorder of the magnetic moments and (ii) the complex interactions between the localized RE-$4f$ electrons and their itinerant counterparts.

In this work, we introduce a theory which attacks these two problems directly. Finite-temperature effects are modeled within the disordered local moment (DLM) [15,16] picture, which is reviewed in Sec. II. Meanwhile, the problematic RE-$4f$ electrons are treated within DFT using the local self-interaction correction (LSIC) [17]. Previous modeling of REs within this framework has been limited to Gd [18–21], but the developments described in Sec. III now allow investigation of the entire RE series for the same computational cost. We use this theory to study the $RECo_5$ family of magnets (Fig. 1), exploring the evolution of magnetism from 0 K (Sec. IV) to T_C (Sec. V). We conclude with our analysis of why, as is observed experimentally, the calculations find $SmCo_5$ to have the highest T_C of the $RECo_5$ magnets (Sec. VI).

II. DFT-DLM APPROACH

At finite temperature, the functional properties of all materials are modified to some extent due to the thermal population of excited vibrational states, e.g., thermal expansion or increased electrical resistivity [22,23]. However, independent of lattice vibrations, the magnetic properties of a material are extremely sensitive to temperature. The disordered local moment (DLM) picture of magnetism provides a conceptual basis to understand this temperature variation [15]. Here, the material is modeled as an array of microscopic magnetic moments (e.g., one associated with each atom), of fixed magnitude but variable orientation. This picture of local moments makes no assumption that the electrons themselves are localized; for example, the $3d$ electrons responsible for magnetism in Fe, the prototypical DLM metal, are completely itinerant [24]. Rather, the spin-spin correlation between electrons near atomic sites can be strong enough to establish magnetically polarized regions which exist for much longer timescales than those associated with electron motion [15]. These are the local moments.

A DLM magnetic microstate is specified by the orientations $\{\hat{e}_i\} = \{\hat{e}_1, \ldots, \hat{e}_N\}$ of the N local moments. The grand potential energy $\Omega(\{\hat{e}_i\})$ is a function of these local moment orientations, and the (classical) statistical mechanics of the system is determined by the partition function

$$Z = \int d\hat{e}_1 d\hat{e}_2 \ldots d\hat{e}_N \exp\left[-\beta\Omega(\{\hat{e}_i\})\right], \qquad (1)$$

where $1/\beta = k_B T$, and T and k_B are the temperature and Boltzmann constant. Experimental measurements correspond to thermal averages over the magnetic microstates. For instance, a magnetization measurement probes the average orientations of the local moments,

$$\langle\hat{e}_j\rangle_T = \frac{1}{Z}\int \hat{e}_j \, d\hat{e}_1 d\hat{e}_2 \ldots d\hat{e}_N \exp\left[-\beta\Omega(\{\hat{e}_i\})\right]. \qquad (2)$$

The DLM paramagnetic state corresponds to each orientation averaging to zero, $\langle\hat{e}_j\rangle_T = 0$, and the highest temperature at which $\langle\hat{e}_j\rangle_T \neq 0$ corresponds to the Curie temperature T_C.

In principle, DFT provides a pathway to a first-principles DLM theory through the possibility of evaluating the grand potential energy $\Omega(\{\hat{e}_i\})$, although finding a sufficiently accurate approximation for the exact exchange-correlation functional remains an ongoing and formidable challenge [25,26]. Specifically, $\Omega(\{\hat{e}_i\})$ could be obtained from constrained DFT calculations, with the applied constraints forcing the local magnetizations to point along designated local moment directions $\{\hat{e}_i\}$) [15]. In practice however, any direct attempt to perform statistical mechanics would soon be faced with the problem of covering the huge phase space spanned by $\{\hat{e}_i\}$, requiring an effectively infinite supercell to contain all N local moments.

A popular method of circumventing this problem is to replace the "exact" Ω with a model, e.g., a Heisenberg model based on pairwise interactions between local moments. The model parameters are extracted from DFT calculations, e.g., from the Liechtenstein formula [27] or constrained DFT [28]. T_C is then obtained from the simpler statistical mechanics of the model, which might be solved through a mean field approach, the random-phase approximation, or Monte Carlo integration [29–33].

These schemes require striking a balance between a model which is sufficiently complex to capture the necessary magnetic interactions, yet simple enough for the statistical mechanics problem to be tractable. The most popular pairwise model should, as its name suggests, only apply when the interaction between two local moments is independent of the alignments of all other local moments in the system. This picture is not particularly intuitive in a metal where one would expect a cooperative effect, i.e., magnetic interactions being reinforced when the material is in a global ferromagnetic state and weakened in the paramagnetic state. Practically, this issue leads to the question of whether one should parametrize the pairwise model for the ferromagnetic or paramagnetic state [27], and what to do at intermediate temperatures [34].

The DFT-DLM theory described in [15] approaches the problem in a different way. Instead of approximating the grand potential energy, one instead introduces an auxiliary quantity $\Omega_0(\{\hat{\boldsymbol{e}}_i\})$ with a known functional form

$$\Omega_0(\{\hat{\boldsymbol{e}}_i\}) = -\sum_i \boldsymbol{h}_i \cdot \hat{\boldsymbol{e}}_i, \tag{3}$$

where the "Weiss fields" $\{\boldsymbol{h}_i\}$ are obtained self-consistently. Specifically, the thermodynamic inequality

$$F(T) \leqslant F_0(T) + \langle \Omega \rangle_{0,T} - \langle \Omega_0 \rangle_{0,T} \tag{4}$$

provides a relation between the exact free energy $F(T)$ and the free energy of the auxiliary system $F_0(T) = -k_B T \ln Z_0$, with

$$Z_0 = \prod_i \int d\hat{\boldsymbol{e}}_i \exp[\boldsymbol{\lambda}_i \cdot \hat{\boldsymbol{e}}_i] = \prod_i \frac{4\pi}{\lambda_i} \sinh \lambda_i \tag{5}$$

and $\boldsymbol{\lambda}_i = \beta \boldsymbol{h}_i$. Crucially, the thermal averages $\langle \ldots \rangle_{0,T}$ appearing in the inequality (4) are calculated with respect to the auxiliary system, e.g.,

$$\langle \Omega \rangle_{0,T} = \frac{1}{Z_0} \prod_j \int d\hat{\boldsymbol{e}}_j \exp[\boldsymbol{\lambda}_j \cdot \hat{\boldsymbol{e}}_j] \Omega(\{\hat{\boldsymbol{e}}_i\}). \tag{6}$$

The Weiss fields are chosen to minimize the right-hand side of the inequality (4). Then,

$$\boldsymbol{h}_i = -\frac{3}{4\pi} \int d\hat{\boldsymbol{e}}_i \langle \Omega \rangle_{0,T}^{\hat{\boldsymbol{e}}_i} \hat{\boldsymbol{e}}_i. \tag{7}$$

The partial average $\langle \Omega \rangle_{0,T}^{\hat{\boldsymbol{e}}_i}$ integrates over all the degrees of freedom in Eq. (6) except the single local moment orientation $\hat{\boldsymbol{e}}_i$. The Weiss fields have the periodicity of the magnetic unit cell, i.e., the number of distinct Weiss fields equals the number of magnetic sublattices.

As indicated by Eq. (7), the Weiss fields are temperature dependent. The DFT-DLM estimate of T_C is the temperature at which all the Weiss fields vanish. Alternatively, one can introduce local order parameters

$$\boldsymbol{m}_i(T) \equiv \langle \hat{\boldsymbol{e}}_i \rangle_{0,T} = \hat{\boldsymbol{\lambda}}_i L(\lambda_i) \tag{8}$$

with $L(\lambda_i) = \coth(\lambda_i) - 1/\lambda_i$. These quantities vary between 1 at zero temperature and 0 at T_C.

We stress that the key quantities in the DFT-DLM theory, the Weiss fields $\{\boldsymbol{h}_i\}$, are calculated with the full grand potential energy Ω, without any assumption on the nature of the underlying interactions, e.g., pairwise, four-spin, etc. [18]. Furthermore, through the averaging in Eq. (7) the magnitudes

of the Weiss fields are indeed influenced by the degree of global order in the system, ensuring self-consistency between $\{\boldsymbol{h}_i\}$ and the "reference state" used to calculate them.

The partial average $\langle \Omega \rangle_{0,T}^{\hat{\boldsymbol{e}}_i}$ appearing in Eq. (7) still presents a challenge to the most widely used implementations of DFT, which solve the Kohn-Sham equations to determine single-particle wave functions [14]. However, the Green's-function-based Korringa-Kohn-Rostoker multiple-scattering formulation of DFT, in combination with the coherent potential approximation (KKR-CPA) [35], allows the partial average to be recast as an impurity problem. This impurity problem, which sees each local moment sitting in an effective medium designed to mimic the averaged properties of the disordered system, can be solved using the same KKR-CPA techniques originally developed to tackle compositional disorder in the simulation of alloys [36]. The DFT-DLM theory has undergone a number of developments from its original formulation, and is being applied to an increasingly wide range of magnetic systems [19–21,37,38]. The practical steps to calculating self-consistent Weiss fields and the key multiple-scattering equations are described in Refs. [16,19,39].

The fact that the DFT-DLM theory is rooted in KKR-CPA has both advantages and disadvantages. Thermally averaged quantities, e.g., spin and orbital moments, can be calculated relatively easily by tracing the relevant operators with the Green's function. The calculations include both core and valence electrons explicitly, and the structure of the KKR-CPA equations allow for a very high degree of numerical precision, e.g., in evaluating integrals over the the Brillouin zone [40]. However, the formalism generally involves making a shape approximation to the Kohn-Sham potential (here we use the atomic sphere approximation, ASA) which, although allowing a compact angular momentum basis to be used to describe the Green's function and scattering matrices, is not expected to perform equally well for cubic and noncubic crystal structures [41]. In addition, we note that DFT-DLM is a mean field theory, with the Weiss fields in Eq. (3) driving the magnetic ordering and vice versa. With these caveats in mind, we expect trends calculated across a series to be more robust than absolute values of specific quantities.

III. SOLVING THE KOHN-SHAM-DIRAC EQUATION WITHIN THE LSIC-LSDA

A. Relativistic DFT-DLM calculations

The large atomic number of the REs necessitates the use of relativistic (R) DFT-DLM theory to describe the spin-orbit coupling inherent in RE-TM magnets as well as mass-velocity and Darwin effects. Practically, our RDFT-DLM calculations involve two steps. In the first step, a self-consistent, scalar-relativistic DFT calculation is performed for a reference magnetic state. This reference magnetic state may be fully ordered (e.g., a ferromagnetic arrangement of spins) or fully disordered (the DLM/paramagnetic state). The output of this calculation is a set of atom-centered potentials. In the second step, these potentials are fed into the fully relativistic Kohn-Sham-Dirac (KSD) equation, thus treating spin-orbit coupling nonperturbatively. Combining the solutions of the KSD equation with the full KKR-CPA machinery allows the Weiss fields and T_C to be computed. Although not a methodological necessity [42],

the potentials here are kept "frozen" in the second step, i.e., the density derived from the Green's function of the partially ordered system is not used to update the potentials.

When constructing the potentials in the first step, in common with all DFT calculations it is necessary to make an approximation for the exchange-correlation energy. The local-spin-density approximation (LSDA) [14,43] performs rather well in describing the magnetism of itinerant electrons, but struggles to describe the strongly localized $4f$ states which characterize REs [44]. Furthermore, the orbital moments of transition metals are generally smaller than observed experimentally when calculated within the LSDA [45]. As a result, it is imperative to go beyond the LSDA exchange correlation when modeling RE-TM magnets.

B. Treating RE-$4f$ electrons

Recent computational works performed at zero temperature have employed charge-self-consistent dynamical mean field theory (DMFT) [46], in particular using the Hubbard-I approximation [47], to calculate the magnetic moments of REs [48] and RE-TM intermetallics like $SmCo_5$ [49–51] and $NdFe_{12}$ [51]. The simpler, "open-core" scheme [52] constrains the total spin density of the RE-$4f$ electrons to be that predicted by Hund's rules [33,50,52–54]. Such calculations, which provide much important insight into RE-TM systems, bear some resemblance to crystal-field theory in the sense that the RE-$4f$ electrons are partitioned from the rest of the material, with the amount of hybridization they can undergo sensitive to how the calculation is set up [51,53]. Alternative approaches like LDA/GGA+U [55–57], the orbital polarization correction (OPC) [58], and the self-interaction correction (SIC) [59] modify the potential at the RE site but treat all electrons equally, in principle allowing the RE-$4f$ states to hybridize freely [55]. An advantage of these schemes when studying trends across the RE-TM series is that, beyond initial choices about how the schemes are implemented, the calculations require minimal user input. Indeed, the parameters entering the OPC and LDA/GGA+U can be calculated from first principles, e.g., the Racah parameters calculated from wave functions in the OPC [45], or the U and J energies calculated from linear response [60] or constrained random-phase approximation calculations [61].

The SIC, which we employ here, aims to ensure that the exchange-correlation potential cancels the electrostatic (Hartree) energy of a single electron interacting with itself, which is not automatically realized in the LSDA [44]. While the scheme becomes more complicated in extended systems, the localized nature of the RE-$4f$ electrons makes them particularly suitable for the SIC [59]. Furthermore, the SIC has already been formulated within the KKR-CPA theory as the local self-interaction correction (LSIC) [17]. Indeed, the LSIC has been previously used in DFT-DLM calculations to study Gd [18–21,38]. However, in order to treat an arbitrary RE it is necessary to generalize the formalism. Conveniently, this same formalism allows the OPC to be also incorporated in the RDFT-DLM framework, facilitating an improved description of the Co orbital moments.
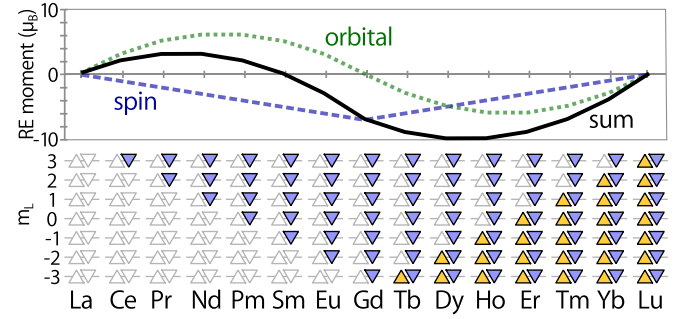

FIG. 2. Scheme to correct RE-$4f$ states based on Hund's rules. Each triangle corresponds to a single spin and orbital angular momentum channel, i.e., $\sigma, l(=3), m$. LSIC channels with $\sigma = \uparrow (\downarrow)$ are represented by yellow (blue) triangles. We also show the moments obtained simply by adding the expectation values of the spin and orbital operators acting on the individual corrected states.

C. An LSIC-LSDA scheme based on Hund's rules

The LSIC formalism [17] is based on applying the self-interaction correction to individual spin and orbital angular channels, each characterized by the pair of quantum numbers σL. σ labels spin, and L is a composite quantum number which, in principle, labels a member of any complete set of angular momentum states. In the original LSIC implementation, these angular momentum states have the same symmetry as the nonmagnetic crystal [17]. However, since the orbital moments are largely unquenched in the RE-TM compounds, here we choose L to label the "atomic" (l,m) quantum numbers associated with the complex spherical harmonics, i.e., eigenfunctions of the orbital angular momentum operator $\hat{l}_z$. As such, states that are degenerate in the nonmagnetic crystal may be split by the LSIC.

We must also choose which spin and orbital angular momentum channels we should apply the LSIC to. We propose to follow the scheme illustrated in Fig. 2, which is inspired by Hund's rules. An extra LSIC channel is added for each RE-$4f$ electron, filling up σL combinations of the same spin ($\downarrow$) first with the largest available opposing m (e.g., $m = +3$ for Ce). After entirely filling the $\downarrow$ channel at Gd, we start filling the $\uparrow$ channel, again starting with the largest available opposing m (e.g., $m = -3$ for Tb) in accordance with the single-electron tendency of orbital and spin momenta to antialign [11]. As shown in Fig. 2, adding up the individual spin and orbital angular momentum contributions associated with these filled states gives quantities symmetric and antisymmetric, respectively, about Gd.

D. Including the LSIC/OPC in the KSD equation

The LSIC scalar-relativistic calculation (the first step referred to in Sec. III A) proceeds as described in Ref. [17]. At the second step in the RDFT-DLM procedure (and at variance with previous work [18–21,38]) the atom-centered potentials have a contribution which depends on angular momentum, conveniently written as

$$V_{\text{SIC}}(\boldsymbol{r}) = \sum_{L,\sigma} V_L^\sigma(r) \hat{P}_{L\sigma}. \tag{9}$$

Here, $V_L^\sigma(r)$ is the spherically symmetric correction to the potential obtained in the scalar-relativistic calculation [17], while $\hat{P}_{L\sigma}$ is a projection operator. In the Pauli representation these operators are 2×2 matrices which are diagonal for spin polarization along the z axis, whose elements project out states with angular momentum character L.

The angular-momentum-dependent potentials result in a modified KSD equation

$$[\tilde{\boldsymbol{\alpha}} \cdot \boldsymbol{p}c + \tilde{V}_{\text{SIC}} + \tilde{I}[V(r) - W] + \tilde{\beta}(\tilde{I}mc^2 + \tilde{\sigma}_z B_{\text{XC}}(r))]\Psi = 0.$$
(10)

Quantities with tildes are 4×4 matrices; Ψ is a bispinor, and W and m the electron energy and rest mass. Compared to the usual KSD equation [62], Eq. (10) has an extra term $\tilde{V}_{\text{SIC}}$, simply related to V_{SIC} in Eq. (9):

$$\tilde{V}_{\text{SIC}} = \begin{pmatrix} V_{\text{SIC}} & 0 \\ 0 & V_{\text{SIC}} \end{pmatrix}.$$
(11)

We now follow the standard method of solving the radial KSD equation in multiple-scattering theory [63], i.e., we investigate the solutions

$$\Psi_\nu^{m_j}(\boldsymbol{r}) = \sum_{\kappa_1} \begin{pmatrix} g_{\kappa_1\nu}^{m_j}(r)\big|\chi_{\kappa_1}^{m_j}\big\rangle \\ if_{\kappa_1\nu}^{m_j}(r)\big|\chi_{-\kappa_1}^{m_j}\big\rangle \end{pmatrix}.$$
(12)

The spin-angular functions $\big|\chi_{\kappa_1}^{m_j}\big\rangle$ are superpositions of the products of Pauli spinors and spherical harmonics weighted by Clebsch-Gordan coefficients [62]. They are characterized by the quantum numbers κ_1 and m_j, and describe the angular character of free-particle solutions of the KSD equation. κ_1 is related to j, the sum of spin and orbital angular momentum in the spin-angular functions, with $\kappa = -l - 1$ for $j = l + 1/2$ and $\kappa' = l$ for $j = l - 1/2$. As indicated, we reserve the label κ for negative values and κ' for positive values of κ_1. The label ν denotes the different solutions required to build the Green's function in scattering theory, i.e., solutions with an asymptotic free-electron character which are regular or irregular at the origin [63].

After inserting the trial solution (12) into Eq. (10) and performing a series of manipulations [62], we obtain coupled equations for the radial functions f and g:

$$\frac{df_{\kappa\nu}^{m_j}}{dr} = \frac{(\kappa - 1)}{r} f_{\kappa\nu}^{m_j} + \frac{1}{\hbar c}(V - E)g_{\kappa\nu}^{m_j}$$
$$+ \frac{1}{\hbar c}\mathcal{G}_+^{m_j}(\kappa,\kappa)g_{\kappa\nu}^{m_j} + \frac{1}{\hbar c}\mathcal{G}_+^{m_j}(\kappa,\kappa')g_{\kappa'\nu}^{m_j},$$

$$\frac{dg_{\kappa\nu}^{m_j}}{dr} = -\frac{(\kappa + 1)}{r} g_{\kappa\nu}^{m_j} + \frac{1}{\hbar c}(E - V + 2mc^2)f_{\kappa\nu}^{m_j}$$
$$+ \frac{1}{\hbar c}\mathcal{G}_-^{m_j}(-\kappa,-\kappa)f_{\kappa\nu}^{m_j}.$$
(13)

Here, $E = W - mc^2$. The differential equations for $f_{\kappa'\nu}^{m_j}$ and $g_{\kappa'\nu}^{m_j}$ are obtained from Eqs. (13) simply by interchanging κ and κ'. Crucially, compared to previous calculations which only included B_{XC}, the basic structure of the coupled equations (13) is unchanged by the addition of V_{SIC}. The difference is in

the coupling functions

$$\mathcal{G}_\pm^{m_j}(\kappa_1,\kappa_2) = \big\langle\chi_{\kappa_1}^{m_j}\big|(\sigma_z B_{\text{XC}} \pm V_{\text{SIC}})\big|\chi_{\kappa_2}^{m_j}\big\rangle.$$
(14)

$B_{\text{XC}}(r)$ is now augmented by a linear combination of the LSIC potentials $V_{(l,m)\sigma}(r)$ weighted by Clebsch-Gordan coefficients. We give the explicit form of these coupling functions in Appendix A, but here just show an example of $\mathcal{G}_\pm^{m_j}(\kappa,\kappa)$ with $\kappa = -4$, $m_j = \frac{1}{2}$:

$$\mathcal{G}_\pm^{1/2}(-4,-4) = \frac{1}{7}B_{\text{XC}} \pm \left[\frac{4}{7}V_{(3,0)}^\uparrow + \frac{3}{7}V_{(3,1)}^\downarrow\right].$$
(15)

We see that the coupling functions can mix occupied, SI-corrected channels with unoccupied, non-SI-corrected channels, as discussed more in Appendix B.

It should be noted that, when deriving the coupled equations (13), additional coupling functions of the form $\mathcal{G}_\pm^{m_j}(-\kappa,\kappa+1)$ are introduced by both σ_z and V_{SIC}. Follow previous work [63] we neglect these terms, which would otherwise result in an infinite ladder of couplings between orbital angular momenta $l, l \pm 2, l \pm 4$, etc. [64].

The coupled equations (13), containing the appropriately weighted LSIC potentials, are solved numerically to give the scattering matrices and regular and irregular contributions to the Green's function. From these quantities, the entire RDFT-DLM computational machinery [39] can be applied without further modification.

The OPC enters the KSD equation in exactly the same way as the LSIC. This is most easily seen by writing the OPC analogy of Eq. (9) as [54,64]

$$V_{\text{OPC}}(\hat{\boldsymbol{r}}) = \sum_{l=2}\sum_{m,\sigma} -B_{l\sigma}m\langle\hat{l}_z\rangle_\sigma \hat{P}_{lm\sigma},$$
(16)

where $B_{l\sigma}$ is a Racah parameter, and $\langle\hat{l}_z\rangle_\sigma$ is the spin-resolved expectation value for the relevant atom (we have anticipated applying the OPC to the d channel). Thus, the OPC can be considered a special case of the LSIC where the potential is independent of r, entering $\mathcal{G}_\pm^{m_j}(\kappa_1,\kappa_2)$ weighted by the coefficients in Appendix A. We stress that, since they only modify the coupling functions, the computational cost of including the LSIC or OPC is negligible.

E. Technical details

We generated the atomic-centered potentials in the fully ordered (zero-temperature) state in self-consistent scalar-relativistic LSIC-LSDA calculations [17,43] within the ASA, as implemented in the HUTSEPOT code [65]. Angular momentum expansions were truncated at $l_{\max} = 3$, and the full Brillouin zone sampled on a $20 \times 20 \times 20$ grid with state occupancies determined by a Fermi-Dirac distribution with an electronic temperature of 400 K. The calculations were performed using experimental lattice constants [10,13], which are listed in Table I together with the ASA radii for the three nonequivalent sites in the RECo$_5$ structure. We used the same relations between ASA radii as in our previous work on YCo$_5$ and GdCo$_5$ [19].

For the RDFT-DLM calculations, apart from the inclusion of the LSIC described above we used the same computational setup (angular mesh, energy contour, electronic temperature) as in [19], including an adaptive sampling of the Brillouin zone [40]. We applied the LSIC to the RE-$4f$ electrons and

TABLE I. Experimental lattice constants, taken from Refs. [10,13]. The ASA radii for the three nonequivalent sites (RE/Co_I/Co_{II}) are also given. All units are in Å.

	a	c	r_{ASA}	Ref.
YCo_5	4.94	3.98	1.83/1.39/1.42	[13]
$LaCo_5$	5.11	3.97	1.91/1.40/1.44	[10]
$CeCo_5$	4.93	4.01	1.83/1.39/1.42	[13]
$PrCo_5$	5.01	3.99	1.86/1.40/1.43	[13]
$NdCo_5$	5.01	3.98	1.86/1.40/1.43	[13]
$SmCo_5$	4.97	3.98	1.85/1.39/1.42	[13]
$GdCo_5$	4.96	3.97	1.85/1.39/1.42	[13]
$TbCo_5$	4.94	3.97	1.84/1.39/1.42	[13]
$DyCo_5$	4.91	3.98	1.82/1.38/1.41	[13]
$HoCo_5$	4.91	3.97	1.82/1.38/1.41	[13]
$ErCo_5$	4.87	4.00	1.81/1.38/1.41	[10]
$TmCo_5$	4.86	4.02	1.81/1.38/1.41	[10]

the OPC to the Co-$3d$ electrons. The magnitude of the OPC was determined iteratively at 0 K with the magnetization aligned along the c axis, updating $\langle \hat{l}_z \rangle_\sigma$ at each iteration to self-consistency. The Racah parameters were calculated scalar relativistically. The same OPC was used for all temperatures, consistent with the frozen-potential approach.

IV. ZERO-TEMPERATURE CALCULATIONS

A. $RECo_5$ moments

We first use the RDFT-DLM formalism to calculate the magnetic moments of the $RECo_5$ series at zero temperature. To illustrate the trend across the lanthanide block, we consider all members of the RE = Y-Lu series, including the nonforming RE = Pm, Eu, Yb, and Lu compounds. Here, we fix the lattice parameters to those of $GdCo_5$; using the appropriate experimental $RECo_5$ lattice parameters (where available) produces very similar zero-temperature moments (Appendix C). For Ce, Pr, and Nd we also performed calculations without applying the LSIC (i.e., treating the f electrons as itinerant).
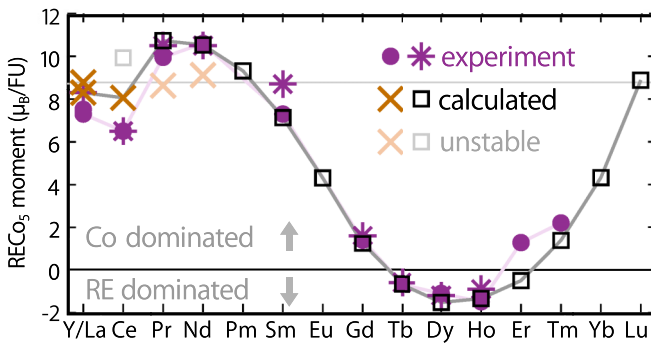

FIG. 3. Magnetic moments calculated at zero temperature with (squares) and without (crosses) the LSIC applied, compared to experimental values reported in Refs. [10] (circles) and [13] (stars). Faint symbols were calculated to be energetically unfavorable. The gray horizontal line at $8.78\mu_B$ corresponds to the calculated YCo_5 moment.

In Fig. 3 we show the calculated $RECo_5$ moments and compare them to low-temperature experiments [10,13]. Here, the Co moments are aligned along the c axis, which defines the positive direction. A negative moment in Fig. 3 therefore means that the RE contribution to the magnetization is larger than that from the Co moments and is pointing in the opposite direction (RE dominated). Usually, experimental measurements (e.g., on powdered samples) only measure the absolute magnetization. However, as we show below, $RECo_5$ compounds which are RE dominated at 0 K show a compensation point (minimum) in their magnetization versus temperature curves, and Ref. [10] reports compensation temperatures for Tb, Dy, and $HoCo_5$. Accordingly, we plot the experimental moments of these three compounds with minus signs.

Considering the calculations without the LSIC first (crosses in Fig. 3) we see relatively small variation for different REs, with the moments fluctuating around the YCo_5 value (shown as the gray horizontal line). We do observe a reduction in moment on moving from YCo_5 to $LaCo_5$, despite both elements having an empty $4f$ shell. In fact, the moment of YCo_5 is much closer to that of $LuCo_5$, whose $4f$ shell is totally filled. This behavior echoes that of quantities like melting points, electronegativities, and ionization energies, which follow more naturally a Sc-Y-Lu series compared to Sc-Y-La [66].

Applying the LSIC (squares in Fig. 3) has a dramatic effect on the magnetization, for instance increasing the moment of $CeCo_5$ by $2\mu_B$/formula unit (FU). Now, a strong variation with RE is observed, with $PrCo_5$/$DyCo_5$ achieving the largest TM/RE-dominated moments, respectively. The transition from TM- to RE-dominated magnetization occurs between Gd and Tb, and back to TM dominated between Er and Tm.

In order to decide whether the calculations with or without the LSIC should be used to describe a given RE, we examine the total energies calculated at the scalar-relativistic level omitting spin-orbit coupling effects. This approach follows, e.g., Refs. [17,67], where the comparison of SIC total energies was used to determine the volume triggering the $\alpha \rightarrow \gamma$ transition in Ce or the valency of the rare earths and their sulphides. We find that applying the LSIC to $PrCo_5$ and $NdCo_5$ lowers the total energy, i.e., it is energetically favorable. Indeed, for heavier REs the non-LSIC calculations become difficult to converge. However, applying the LSIC to $CeCo_5$ *increases* the scalar-relativistic total energy, indicating that the single Ce-$4f$ electron would prefer to be delocalized in this compound. Using this total energy as our criterion, we do not apply the LSIC to $CeCo_5$. Indeed, the picture of the itinerant Ce-$4f$ electron has already been established in previous theoretical work [68]. Other nonenergetically favorable calculations are shown in Fig. 3 as faint symbols.

The variation in $RECo_5$ moment calculated with the LSIC largely follows the simple picture presented in Fig. 2. In general, the antiferromagnetic RE-TM exchange interaction causes the RE spin moments to point in the opposite direction to the Co moments [69], but whether or not the *total* RE moment aligns parallel or antiparallel depends on the sign and magnitude of the orbital contribution [70]. The lightest REs have large orbital components pointing opposite to their spin which leads to parallel alignment of the total moments, whereas the spin and orbital moments of the heavy REs always reinforce each other to give antiparallel alignment.

TABLE II. Decomposition of zero-temperature moments. All quantities are in μ_B. For comparison, we include the calculations for CeCo$_5$ with the LSIC applied (*) even though it is energetically unfavorable.

	RE moment (spin/orbital/total)	Scalar rel. spin (f/spd)	Co moment (spin/orbital/total)	Total moment/FU	Exp. [10]	Exp. [13]
YCo$_5$	$-0.31/0.04/-0.28$	$-0.31\ (0.00/-0.31)$	$7.54/1.25/8.78$	8.50	7.52	8.3
LaCo$_5$	$-0.30/0.04/-0.26$	$-0.30\ (-0.04/-0.25)$	$7.11/1.19/8.30$	8.04	7.3	
CeCo$_5$	$-0.92/0.51/-0.41$	$-0.86\ (-0.57/-0.29)$	$7.07/1.40/8.47$	8.06	6.5	6.5
CeCo$_5$*	$-1.37/2.97/1.60$	$-1.37\ (-1.07/-0.30)$	$7.19/1.14/8.33$	9.93	6.5	6.5
PrCo$_5$	$-2.46/4.88/2.42$	$-2.47\ (-2.13/-0.34)$	$7.25/1.06/8.31$	10.73	9.95	10.5
NdCo$_5$	$-3.56/5.74/2.18$	$-3.58\ (-3.22/-0.37)$	$7.33/1.02/8.35$	10.53	10.6	10.5
PmCo$_5$	$-4.63/5.60/0.97$	$-4.71\ (-4.32/-0.39)$	$7.38/0.97/8.35$	9.32		
SmCo$_5$	$-5.63/4.55/-1.08$	$-5.82\ (-5.41/-0.40)$	$7.36/0.85/8.21$	7.13	7.3	8.7
EuCo$_5$	$-6.60/2.60/-4.01$	$-6.90\ (-6.48/-0.42)$	$7.36/0.95/8.32$	4.31		
GdCo$_5$	$-7.50/0.03/-7.47$	$-7.49\ (-7.00/-0.49)$	$7.43/1.27/8.70$	1.23	1.37	1.6
TbCo$_5$	$-6.42/-2.96/-9.38$	$-6.41\ (-5.98/-0.44)$	$7.44/1.28/8.72$	-0.67	-0.68	-0.6
DyCo$_5$	$-5.33/-4.93/-10.26$	$-5.32\ (-4.93/-0.39)$	$7.46/1.28/8.75$	-1.52	-1.1	-1.2
HoCo$_5$	$-4.26/-5.88/-10.14$	$-4.20\ (-3.86/-0.34)$	$7.51/1.29/8.80$	-1.34	-1.49	-0.9
ErCo$_5$	$-3.28/-5.89/-9.17$	$-3.09\ (-2.78/-0.31)$	$7.40/1.27/8.67$	-0.50	1.28	
TmCo$_5$	$-2.27/-4.92/-7.19$	$-2.00\ (-1.71/-0.29)$	$7.32/1.25/8.57$	1.38	2.2	
YbCo$_5$	$-1.26/-2.95/-4.22$	$-0.92\ (-0.65/-0.27)$	$7.30/1.24/8.53$	4.32		
LuCo$_5$	$-0.29/0.04/-0.25$	$-0.30\ (-0.03/-0.27)$	$7.59/1.29/8.88$	8.63		

B. Decomposition of RECo$_5$ moments

In Table II we resolve the calculated moments into spin and orbital contributions from the RE and TM. We also give the spin moments calculated at the scalar-relativistic level, which are further resolved into contributions of different angular momentum (f or spd) character.

Concentrating first on the RE contribution to the magnetization, we see that the spin moments roughly track the expected spin of the LSIC channels, peaking at Gd. The scalar-relativistic decomposition shows the spin moments have an spd component which increases from $0.25\mu_B$ for La to $0.49\mu_B$ for Gd. However, the f components of the spin moment are not simply integers. Based on the simple picture of Fig. 2, this observation is surprising since we would expect each localized RE-4f electron to contribute $\pm 1\mu_B$ to the magnetization. Instead, we see that for each additional LSIC channel the change in f components is closer to $\pm 1.1\mu_B$, until the elements with filled spin subshells (GdCo$_5$ and LuCo$_5$) are reached. This behavior indicates that the nominally unoccupied RE-4f states, which do not have the LSIC applied, are affecting the calculated properties.

The RE orbital moments also follow the general trend of Fig. 2, but are better described by $\mu_o = (2 - g_J)J$, where g_J is the Landé factor [71]. This textbook expression is obtained by projecting the orbital moment onto the total angular momentum direction, which is valid for strong spin-orbit coupling. It is therefore natural to ask whether the spin RE moments should in fact be described by $\mu_s = 2(g_J - 1)J$, which is the corresponding projection for spin [71]. However, in our calculations the principal interaction affecting the spin moments is the scalar-relativistic exchange, which can be confirmed by noting the close agreement between the RDFT-DLM and scalar-relativistic spin moments in Table II. Therefore, the spin-orbit interaction plays a relatively minor role in determining the spin moment and the considerations leading to μ_s do not apply. We note that this situation is

qualitatively different to the open-core scheme [52], which fixes the RE spin moments to μ_s.

Now, considering the TM contribution to the magnetization, the most striking feature in Table II is the different behavior of the light and heavy RECo$_5$ compounds. The Co moments exhibit relatively small variations for the heavy REs except for LuCo$_5$ which, as already noted, behaves similarly to YCo$_5$. However, the variations for the light REs are much larger. Moving from La to Eu, the Co spin and orbital moments increase and decrease, respectively, and in general the total Co moments are smaller than for the heavy RECo$_5$ compounds. As we discuss in Sec. V, a qualitative difference in light and heavy RECo$_5$ behavior is also observed in T_C.

C. Comparison to experiment

When comparing to experiment, it is important to note that there is a sizable scatter in the published data. We have taken experimental low-temperature moments from the review articles of Refs. [10,13] which agree reasonably well with each other except for YCo$_5$ and SmCo$_5$, which deviate by approximately $1\mu_B$. Also, we note that the RE = Tb-Tm compounds do not form with exact RECo$_5$ stoichiometry. Instead, due to defects where the RE is substituted with pairs (dumbbells) of Co atoms [72], the compounds become increasingly Co rich. For example, the actual stoichiometry of the RE = Tm compound reported in Ref. [10] is TmCo$_6$.

With these limitations in mind, the calculations compare reasonably well to experiment in Fig. 3. Certainly, a number of qualitative features are reproduced, e.g., a drop in moment from Y to La, a large increase from Ce to Pr, and RE-dominated magnetization for Tb-Ho.

For the special case of CeCo$_5$, we note that the energetically unstable LSIC calculation gives a moment which is in qualitative disagreement with the experimental trend. Interestingly, however, while the LSDA+OPC calculations are closer to
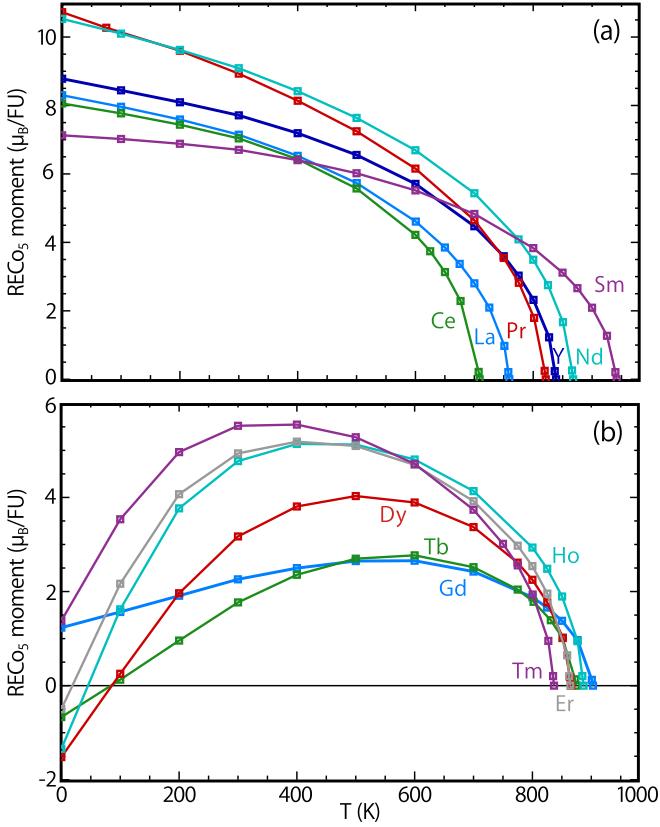
FIG. 4. Magnetization per formula unit calculated at different temperatures for the (a) light and (b) heavy $RECo_5$ compounds. Calculations were performed at the $GdCo_5$ lattice parameters.

experiment, they still overestimate the $CeCo_5$ moment. Not including the OPC on the Co atoms rather improves the agreement (Ref. [68] and Appendix C), suggesting that (like for the LSIC) there might be a criterion based on energetics to decide whether or not the OPC should be applied.

Apart from the cases of $ErCo_5$ and $TmCo_5$ where the experiments are Co rich, the remaining compound where the discrepancy between calculations and experiment is quite large is $SmCo_5$, specifically compared to the value of $8.7\mu_B$/FU in Ref. [13]. Interestingly, a recent neutron diffraction experiment reported even larger local moments in $SmCo_5$, which add up to give a resultant magnetization in excess of $12\mu_B$/FU [73]. Studies employing DMFT and open-core calculations have reported smaller Sm total moments of approximately $-0.3\mu_B$, which would bring the total $SmCo_5$ moment closer to $8\mu_B$/FU [49–51]. Earlier GGA+U calculations found a much larger total moment of $9.9\mu_B$/FU due to a ferromagnetic alignment of Sm and Co spins. The scatter in theoretical and experimental data hints at the richness of the physics of $SmCo_5$ which, as we show next, is also seen in T_C.

V. FINITE-TEMPERATURE CALCULATIONS

A. Magnetization vs temperature curves

We now include local moment disorder within the RDFT-DLM picture. Figures 4(a) and 4(b) show the magnetization versus temperature (MvT) curves calculated for light and

heavy $RECo_5$ compounds. These calculations were performed at the $GdCo_5$ lattice constants (Table I). The light REs show behavior associated with ferromagnets, i.e., a monotonic decrease in magnetization with increasing temperature. By contrast, the heavy $RECo_5$ compounds have magnetizations which initially become more positive (TM dominated) as the temperature increases, before reducing at higher temperatures. As we have shown previously by comparing YCo_5 and $GdCo_5$ [19], this contrasting behavior is due to the RE moments disordering more quickly with temperature compared to the antiferromagnetically aligned Co sublattice. As a result, the strong negative contribution to the total magnetization from the heavy RE diminishes quickly, leaving the positive Co magnetization.

In the case that the zero-temperature magnetization is RE dominated, there is a compensation temperature at which the strongly disordered RE magnetization cancels the weakly disordered Co magnetization. Our calculated compensation temperatures are 84 K ($TbCo_5$), 85 K ($DyCo_5$), 45 K ($HoCo_5$), and 19 K ($ErCo_5$). Reference [10] reports experimental compensation temperatures of 110 K ($TbCo_5$), 123 K ($DyCo_5$), and 71 K ($HoCo_5$).

We note that the calculated MvT curves have finite slopes at $T = 0$ K, while experimentally measured curves tend to be flat [19]. The origin of this discrepancy is the classical statistical mechanics used in the DLM picture [Eq. (3)], which does not give an energy barrier between the zero-temperature arrangement of local moments and an excited state where the moments have undergone infinitesimal rotations.

B. RE order parameters

In order to analyze the RE contribution to the magnetization in more detail, in Figs. 5(a) and 5(b) we plot the temperature evolution of the RE order parameter m_{RE} [Eq. (8)]. The heaviest REs Ho, Er, and Tm disorder very quickly with temperature, losing 50% of their ordering below 200 K. By contrast, the Sm sublattice retains its ordering to much higher temperatures, e.g., 50% ordering at 650 K. Although part of the reason for this behavior is the higher T_C of $SmCo_5$, plots of the order parameter against reduced temperature T/T_C (not shown) demonstrate that even when this factor is accounted for, Sm orders the most strongly.

Having an ordered RE at high temperature is useful for permanent magnets since the magnetocrystalline anisotropy decays faster than m_{RE} [9]. Therefore, $SmCo_5$ has a double advantage of having a high magnetocrystalline anisotropy at low temperature, and a strong RE ordering to retain this anisotropy at high temperature.

C. Curie temperatures

In Fig. 6(a) we compare the calculated Curie temperatures T_C (extracted from Fig. 4) to the experimental values reported in Ref. [10]. We include T_C calculated for the nonforming Pm, Eu, Yb, and $LuCo_5$ compounds. We remind the reader that experimental values are for Co-rich heavy $RECo_5$ compounds, for which we would expect an increased T_C. For instance, the measured T_C of Gd_2Co_{17} is 200 K higher than $GdCo_5$ [10].
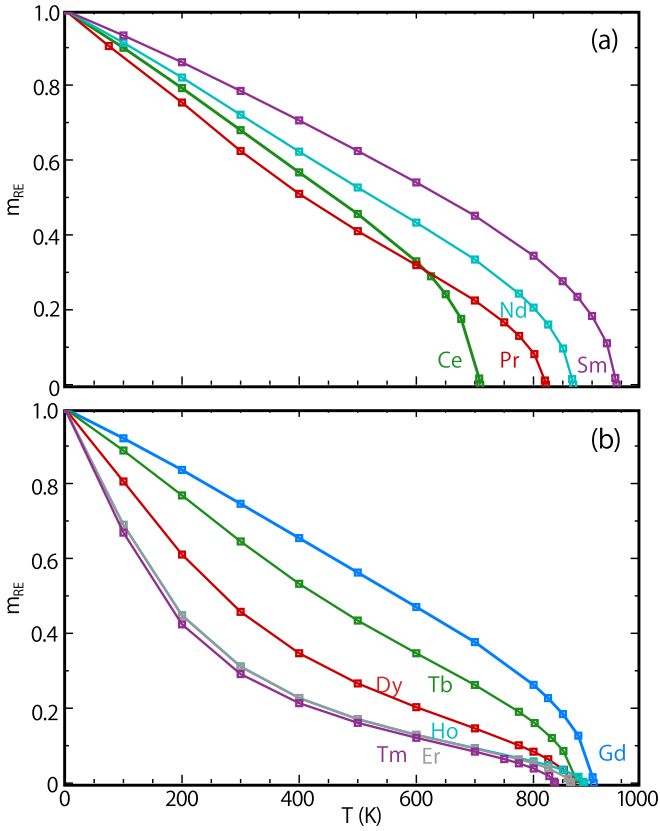
FIG. 5. RE order parameters m_{RE} [Eq. (8)] from the calculations of Fig. 4 on the light (a) and heavy (b) RECo$_5$ compounds.

FIG. 6. (a) T_C calculated for RECo$_5$ using the GdCo$_5$ lattice parameters, compared to the experimental values reported in Ref. [10] (circles). Squares and crosses are calculated with and without the LSIC, respectively, and the faint square is the energetically unfavorable LSIC calculation for CeCo$_5$. (b) Comparison of T_C calculated for GdCo$_5$ using RECo$_5$ lattice parameters (circles), RECo$_5$ using GdCo$_5$ lattice parameters (squares), and RECo$_5$ using RECo$_5$ lattice parameters (crosses). The faint gray lines separate light and heavy REs.

Figure 6(a) clearly shows the contrasting behavior of the light and heavy RECo$_5$ compounds. Apart from YCo$_5$ and CeCo$_5$, the T_C of the light RECo$_5$ compounds increases monotonically with the number of RE-4f electrons. Indeed, applying the energetically unfavorable LSIC to the Ce-4f electron also causes CeCo$_5$ to follow this trend [faint square in Fig. 6(a)]. Of the experimentally known RECo$_5$ compounds, SmCo$_5$ is calculated to have the highest T_C (942 K), but the T_C of the nonforming EuCo$_5$ compound is found to be even higher, at 973 K.

The trend in calculated T_C of the heavy RECo$_5$ compounds is less obvious. In general, filling the remaining subshell causes a reduction in T_C, but a secondary peak is observed at HoCo$_5$. This peak in T_C coincides with a slight peak in Co moments for HoCo$_5$ at zero temperature (Table II). Also, the T_C of LuCo$_5$ is very close to that calculated for YCo$_5$ (850 and 839 K, respectively).

The calculations and experiments agree on a number of qualitative features. First, there is a substantial drop in T_C on moving from YCo$_5$ to LaCo$_5$, and another from LaCo$_5$ to CeCo$_5$. As already noted, the drop for CeCo$_5$ is not observed if the Ce-4f electron is localized with the LSIC. Second, SmCo$_5$ has the highest T_C of all the experimentally attainable RECo$_5$ compounds. Finally, the Co-rich heavy RECo$_5$ compounds do show a secondary peak in T_C like the calculations, although at Er not Ho. The heavy RE$_2$Co$_{17}$ compounds, whose stoichiometry is better defined, also show a secondary peak around Ho/Er/Tm followed by a sharp upturn for Lu [10].
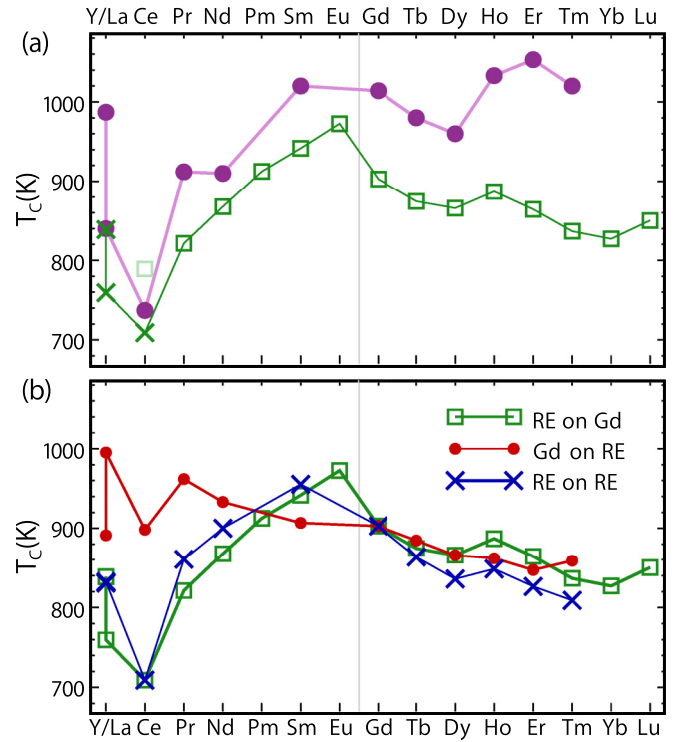
The calculated variation in T_C shown in Fig. 6(a) is only due to changing the RE. In order to quantify the magnetostructural effect of varying the lattice, we also calculated T_C for the RECo$_5$ compounds using experimentally reported lattice parameters (Table I). We further performed calculations where we varied the lattice but fixed the RE to Gd, i.e., GdCo$_5$ on different RECo$_5$ lattices. We compare the three different sets of calculations in Fig. 6(b).

First considering the calculations with the RE fixed to Gd [red circles in Fig. 6(b)], we observe a decrease in T_C across the lanthanide block. The exception is CeCo$_5$, which shows a strong magnetostructural effect; as shown in Table I, CeCo$_5$ has an anomalously small a parameter. These calculations do not reproduce experimental trends, e.g., predicting LaCo$_5$ to have the highest T_C.

If instead we vary both the RE and the lattice parameters [blue crosses in Fig. 6(b)] we find an almost identical trend in T_C as if we had kept the lattice parameters fixed at GdCo$_5$ (green squares). Using the RECo$_5$ lattice parameters accentuates the drop in T_C for CeCo$_5$. Unfortunately, the experimentally observed difference in T_C between YCo$_5$ and LaCo$_5$ is no longer calculated, which can be seen as a cancellation of competing green and red symbols in Fig. 6(b). In general, the calculations find magnetostructural effects to play

a less important role in determining T_C than explicitly varying the RE.

D. Order-parameter expansion of the free energy

Returning to the calculations with the lattice constants fixed to GdCo$_5$, to gain further insight into the calculated T_C we expand the RDFT-DLM potential energy $\langle \Omega \rangle_{0,T}$ in terms of the order parameters m_{RE}, $m_{\mathrm{Co_I}}$, and $m_{\mathrm{Co_{II}}}$ [19]. The labels I and II distinguish between the inequivalent Co positions in the RECo$_5$ structure (Fig. 1), i.e., the two Co atoms in plane with the RE (Co$_I$, Wyckoff position $2c$) and the three out-of-plane Co atoms (Co$_{II}$, Wyckoff position $3g$). In this expansion, the Weiss field at each site $(h_{\mathrm{RE}}, h_{\mathrm{Co_I}}, h_{\mathrm{Co_{II}}})$ is given by the equation

$$\begin{pmatrix} h_{\mathrm{RE}} \\ 2h_{\mathrm{Co_I}} \\ 3h_{\mathrm{Co_{II}}} \end{pmatrix} = \begin{pmatrix} J_{\mathrm{RE\text{-}RE}} & J_{\mathrm{RE\text{-}Co_I}} & J_{\mathrm{RE\text{-}Co_{II}}} \\ J_{\mathrm{RE\text{-}Co_I}} & J_{\mathrm{Co_I\text{-}Co_I}} & J_{\mathrm{Co_I\text{-}Co_{II}}} \\ J_{\mathrm{RE\text{-}Co_{II}}} & J_{\mathrm{Co_I\text{-}Co_{II}}} & J_{\mathrm{Co_{II}\text{-}Co_{II}}} \end{pmatrix} \begin{pmatrix} m_{\mathrm{RE}} \\ m_{\mathrm{Co_I}} \\ m_{\mathrm{Co_{II}}} \end{pmatrix}. \tag{17}$$

The prefactors in the Weiss fields account for the site multiplicities. The expansion of Eq. (17) is valid for small m, i.e., close to T_C. The coefficients J_{XY} are obtained by least-squares fitting of RDFT-DLM calculations. As discussed in Ref. [19], diagonalization of the matrix in Eq. (17) gives the RDFT-DLM T_C, thus allowing the variation shown in Fig. 6(a) to be understood in terms of the strength of the interactions between different magnetic sublattices.

The calculated coefficients J_{XY} are shown in Fig. 7. A negative J_{XY} indicates a tendency for the spins of species X and Y to align antiferromagnetically. Comparing Figs. 6(a) and 7, we see that the behavior of T_C is mirrored by the largest J_{XY} coefficient $J_{\mathrm{Co_I\text{-}Co_{II}}}$, which describes the interlayer Co interaction. The next-largest coefficient $J_{\mathrm{Co_{II}\text{-}Co_{II}}}$, describing the intralayer interactions of the pure Co layer, behaves similarly except that no drop at CeCo$_5$ is observed. It is not surprising either that T_C tracks the largest J_{XY} coefficients or that these coefficients describe Co-Co interactions, in line with the picture that the TM is responsible for the high T_C in RE-TM magnets. What is less intuitive is that these coefficients should be so strongly affected by the RE.

As found for T_C, there is clear distinction between light and heavy RECo$_5$ compounds for $J_{\mathrm{Co_I\text{-}Co_{II}}}$ and $J_{\mathrm{Co_{II}\text{-}Co_{II}}}$. By contrast, $J_{\mathrm{Co_I\text{-}Co_I}}$ undergoes a general decrease from La-Lu, with slight fluctuations around Ho and a dip at Ce. The Co interactions are very similar for Y and Lu, consistent with their similar T_C.

The $J_{\mathrm{RE\text{-}Y}}$ coefficients which quantify RE interactions are smaller in magnitude. $J_{\mathrm{RE\text{-}RE}}$ is particularly weak and correlates with the size of the spin moment of the RE. The strongest RE-Co interactions are interplanar, RE-Co$_{II}$. Interestingly, neither $J_{\mathrm{Co_{II}\text{-}Co_{II}}}$ nor $J_{\mathrm{RE\text{-}Co_{II}}}$ show any strong anomaly at CeCo$_5$, indicating that it is only the Co$_I$ interactions which are affected by the itinerant Ce-$4f$ electron.

Again comparing the light and heavy REs, we note that the in-plane interaction quantified by $J_{\mathrm{RE\text{-}Co_I}}$ actually becomes ferromagnetic for DyCo$_5$, HoCo$_5$, and ErCo$_5$, which coincides with the secondary peak in T_C [Fig. 6(a)]. Also, we observe that the strongest RE-Co interactions occur not for GdCo$_5$, which has the largest RE spin moment, but rather EuCo$_5$.
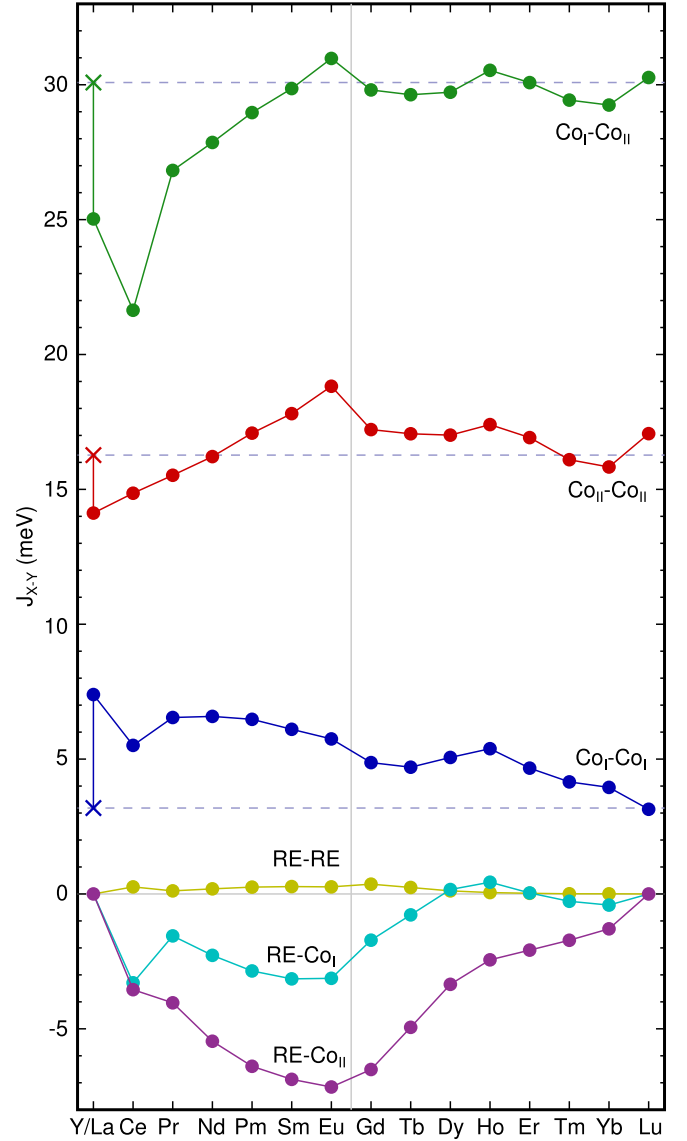

FIG. 7. Different J_{XY} parameters [cf. Eq. (17)] calculated for RECo$_5$ on the GdCo$_5$ lattice. Note that the Ce calculation was performed without the LSIC, i.e., assuming that the Ce f electron is itinerant. We highlight J_{XY} for YCo$_5$ as crosses with horizontal dashed lines.

VI. DISCUSSION

A. RE-TM interaction

Our calculations have found that the strength of magnetic interactions between Co moments in RECo$_5$ is affected by the RE, even when the lattice parameters are held fixed. As a result of this variation, T_C depends heavily on the RE. To explain this behavior, we first recall the theory of RE-TM interactions described in Ref. [69], which explains the antiferromagnetic spin coupling in terms of hybridization between RE-$5d$ and TM-$3d$ states. Figure 8 is a schematic representation of the theory. The magnetic properties of Co originate from almost-full and almost-empty $3d$ bands of opposing spins. The minority spin Co-$3d$ band lies closer in energy to the RE-$5d$ bands than the majority Co-d band, and therefore hybridizes more strongly. The preferential occupation of the lower-energy
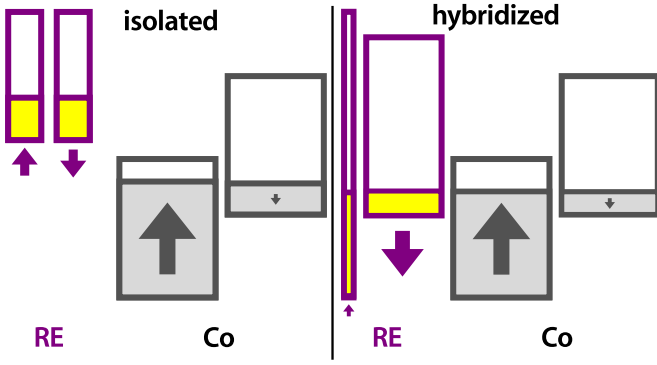
FIG. 8. Schematic of antiferromagnetic RE-Co interaction, after Fig. 2 of Ref. [69]. Wide/narrow rectangles symbolize strong/weak RE-Co hybridization in a given spin channel.

hybridized spin states causes the RE-5d bands to develop a spin polarization in the direction of the Co minority spin, i.e., an antiferromagnetic coupling. Then, onsite RE 4f-5d interactions polarize the RE-4f spins in the same sense.

In this picture, the RE-TM interaction varies according to the strength of the 4f-5d interaction, which is expected to scale with the spin moment of the RE. Accordingly, the strongest RE-TM interactions are expected for Gd. However, any effects on the TM magnetization are expected to proceed via the Co-3d–RE-5d hybridization, with no direct link to the RE-4f states.

B. Magnetostructural effects

Within the picture of Fig. 8, any variation in T_C implies that the RE-5d states are not the same for all REs. Of course, the RE-5d orbitals do vary across the lanthanide block in terms of their spatial extent, as can be seen from the experimental lattice parameters in Table I. The lattice parameter a of LaCo$_5$ is 3% larger than GdCo$_5$, while for YCo$_5$ the difference is less than 0.5%. The experimental lattice parameters of LuCo$_5$ are not known, but the ionic radius of Lu is much closer to Y than La [74]. Correspondingly, the T_C values calculated at GdCo$_5$ lattice parameters are much closer for YCo$_5$ and LuCo$_5$ (11 K) than YCo$_5$ and LaCo$_5$ (80 K).

So, independent of any arguments based on the RE-4f states, the calculations on YCo$_5$, LaCo$_5$, and LuCo$_5$ suggest that the size of the RE-5d orbitals affects the Co magnetism. Indeed, we could have reached a similar conclusion from our calculations on GdCo$_5$ with variable lattice parameter. Using the lattice parameters of lighter (heavier) RECo$_5$ compounds for GdCo$_5$ corresponds to expansion (compression) of a (Table I). From the red line of Fig. 6(b), we see that expansion of a is correlated with an increased T_C, while compression reduces it. Inversely, using GdCo$_5$ lattice parameters for the light and heavy RECo$_5$ compounds corresponds to compression and expansion of a, respectively. Comparing the green and blue symbols in Fig. 6(b) confirms that compression reduces T_C (green lower than blue for La-Gd) while expansion increases T_C (green higher than blue for Gd-Tm).

This magnetostructural effect makes some contribution to the overall variation of T_C. Interestingly, the coefficients in Fig. 7 which quantify the Co$_I$-Co$_I$ interaction (blue symbols) resemble the behavior of T_C calculated for GdCo$_5$ with

different lattice parameters [red symbols in Fig. 6(b)]. Taken together with the fact that these Co$_I$ atoms sit in plane with the RE atoms (Fig. 1), we assert that the variation $J_{Co_I\text{-}Co_I}$ is magnetostructural in origin, with the RE-5d orbitals affecting the in-plane Co-3d interactions.

However, magnetostructural effects cannot really explain the observed variation in T_C. First, they do not account for the qualitative difference in behavior between light and heavy RECo$_5$ compounds. Second, the $J_{Co_I\text{-}Co_I}$ coefficients which are sensitive to the structure do not play a major role in determining T_C, compared to $J_{Co_I\text{-}Co_{II}}$ and $J_{Co_{II}\text{-}Co_{II}}$. For example, LaCo$_5$ has the largest $J_{Co_I\text{-}Co_I}$ but the second lowest T_C [Fig. 6(a)]. Therefore, we look for an additional explanation.

C. Densities of states

In Fig. 9(a) we plot the DFT Kohn-Sham density of states (DOS) of SmCo$_5$. The DOS was calculated just below T_C (i.e., at an almost completely disordered state), using GdCo$_5$ lattice parameters, and has been resolved into contributions from the RE, Co$_I$, and Co$_{II}$ sublattices. The wide energy scale of Fig. 9(a) was chosen to show explicitly the energy position of the occupied Sm-4f states, 11 eV below the Fermi level E_F. Zooming in on the region around E_F [Fig. 9(b)] shows the Co-3d band (bandwidth ∼4 eV) hybridized with the RE-5d states. However, an additional prominent feature is observed in the RE DOS, which is a narrow peak above E_F. The weight of this peak is approximately two electrons, and corresponds to the two unoccupied RE-4f states in the $\downarrow$ spin channel (Fig. 2).

A similar peak can be observed in the DOS of all the RECo$_5$ compounds. For REs with almost empty 4f spin subshells, the peak is located at high energy, and comes closer to E_F as the subshell becomes filled.[1] We stress that in our DFT description, states above E_F make no contribution to calculated properties. However, the tail of this unoccupied RE-4f peak does extend below E_F and therefore contributes to the density. In fact, this tail is the origin of the noninteger contribution to the f-resolved spin moments pointed out in Sec. IV B when discussing Table II.

As indicated in Fig. 9(b), we can extract the energy corresponding to the center of this unoccupied peak (dashed line). Then, in Fig. 9(c) we plot the calculated T_C as a function of this peak position. The light REs show an apparently strong correlation, with T_C increasing as the unoccupied peak becomes closer to E_F. By contrast, the heavy REs do not show any particular correlation. The possible exception is HoCo$_5$, which as well as having a higher T_C than its neighbors also has the unoccupied RE-4f peak closest to E_F.

An explanation for the differing behavior of the light and heavy RECo$_5$ compounds in Fig. 9(c) relates to the spin character of the unoccupied peak. For the light REs, the unoccupied RE-4f peak closest to E_F has the same $\downarrow$ spin as the Co-3d minority spins, i.e., the states which hybridize strongly with the RE-5d states and lead to antiferromagnetic coupling (Fig. 8). By contrast, the unoccupied RE-4f peak of the heavy REs has the same $\uparrow$ spin character as the Co-d

---

[1]For light REs, a second peak corresponding to the opposite spin channel is also present, at much higher energies.
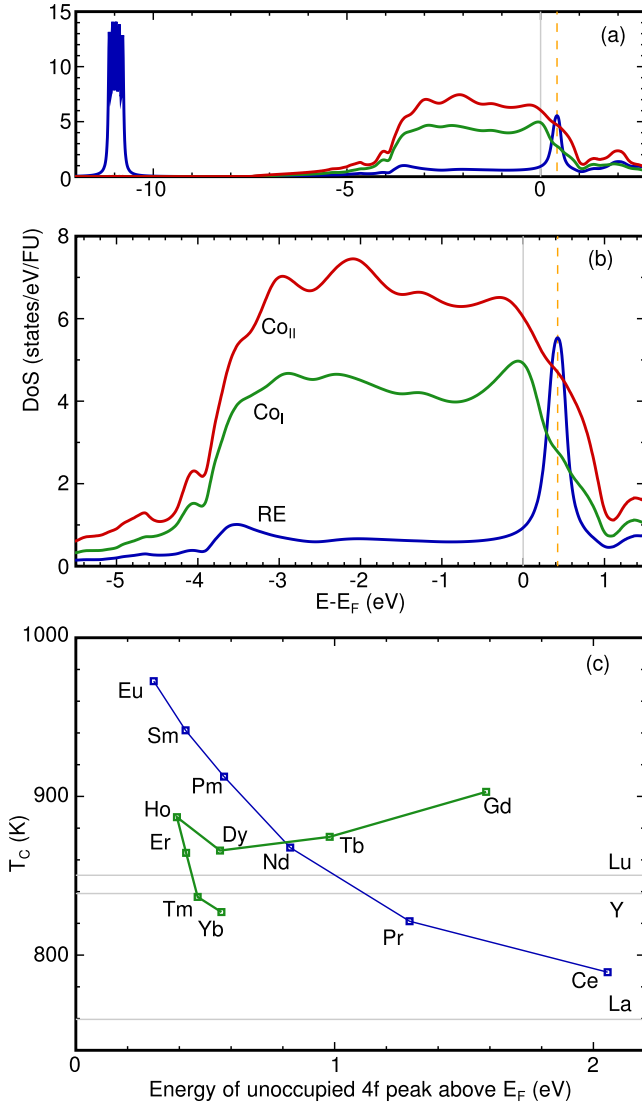
FIG. 9. DOS calculated just below T_C for SmCo$_5$, resolved onto the Sm, Co$_I$, and Co$_{II}$ sublattices, shown (a) across a wide energy scale and (b) around the Fermi energy. The vertical dashed line intersects the center of the unoccupied $4f$ peak above the Fermi energy. (c) T_C plotted against the center of this unoccupied peak for the different RECo$_5$ compounds. Note that here the value of T_C of CeCo$_5$ was calculated with the LSIC applied.

majority spins. The hybridization of these states with RE-$5d$ is weak due to the energy separation; also, it favors ferromagnetic coupling. As noted when discussing Fig. 7, HoCo$_5$ does indeed have a positive $J_{\text{RE-Co}_I}$ coefficient, corresponding to a ferromagnetic RE-TM interaction. Indeed, the temperature evolution of the order parameters in Fig. 5 shows how the overall antiferromagnetic RE-TM coupling is weakened for the heavy RECo$_5$ compounds.

We therefore propose a mechanism where a small contribution of f-character RE states, located just below the Fermi level, affects T_C by modifying the Co-$3d$ states, probably indirectly through the RE-$5d$ states. Such a mechanism could explain why we calculate higher T_C's than GdCo$_5$ for Pm, Sm, and EuCo$_5$, despite these elements having smaller spin

moments and being placed on a lattice with a compressed a parameter. The effect is strong (weak) for the light (heavy) RECo$_5$ compounds, and favors antiferromagnetic (ferromagnetic) RE-TM coupling as described above, consistent with the behavior of $J_{\text{RE-Co}_I}$ and $J_{\text{RE-Co}_{II}}$ shown in Fig. 7.

We have already pointed out that the calculations have found SmCo$_5$ both to have the highest T_C of the experimentally realized RECo$_5$ compounds and also a strong RE-TM interaction, which enables Sm to stay ordered at high temperature. Within the mechanism described here, the origin of this behavior is Sm's almost-filled $4f$ spin subshell. The hypothetical EuCo$_5$ compound would have an even higher T_C, but unfortunately does not form. The total energies calculated at the scalar-relativistic level find Eu to be more stable in the 3+ state than 2+, when forced to occupy the RECo$_5$ structure. However, we have not investigated the full compositional phase diagram where different stoichiometries and structures might have a lower free energy.

VII. OUTLOOK

We have devised a physically transparent theory to model the magnetic properties of RE-TM compounds, with particular emphasis on their finite-temperature properties. The magnetic disorder is described with the disordered local moment picture based on relativistic density functional theory, with the RE-$4f$ electrons treated with the local self-interaction correction which encapsulates Hund's rules. We used the theory to calculate the zero- and finite-temperature properties of the RECo$_5$ family of magnets, comparing magnetic moments and Curie temperatures to experimental measurements.

When presenting our theory we stated that, mainly as a result of the spherical approximations and mean field nature of the theory, we expected our approach to perform best in calculating trends across a series. This statement has been borne out by our comparisons with experimental data, where we were able to reproduce a number of qualitative features. In particular, we were able to track the behavior of T_C, which to our knowledge has never been accomplished from first principles before.

We identified interesting behavior from the calculations, that even though T_C is generally determined by TM-TM interactions, these interactions were nonetheless affected by the RE. We argued that while the varying spatial extent of the RE-$5d$ orbitals did affect the TM-TM interactions, this effect was not sufficient to explain the variation in T_C. Instead, we proposed a mechanism based on a small f-character contribution to the density around the Fermi level which, for the light RECo$_5$ compounds, strengthens both the RE-TM and TM-TM interactions.

We note that more expensive DMFT calculations do not provide an obvious pathway for a further exploration of this mechanism, neither in being able to calculate T_C, nor also since we cannot make any assumptions about the hybridization of the RE-$4f$ electrons [51]. In terms of experimental evidence, we currently have only the observation that SmCo$_5$ has a higher T_C than GdCo$_5$. To our knowledge, this observation has not been explained before, but on its own cannot be considered justification for the correctness of the LSIC. However, the theory presented here opens the door to performing a more detailed comparison with experimental measurements on the

temperature-dependent properties of any RE-TM compound, as was already done for YCo$_5$ and GdCo$_5$ [19].

Beyond exploring the fundamental physics of RE-TM magnets, our theoretical framework allows the study of practical aspects. In particular, the CPA formalism allows the effects of compositional disorder, e.g., substitution of RE or TM elements, to be investigated. Furthermore, with a view to optimizing high-temperature coercivity, it is highly desirable to tackle the temperature dependence of the magnetocrystalline anisotropy [37]. Such calculations require a careful incorporation of crystal-field effects into our ASA calculations [75] and also special care regarding how the calculated quantities are compared to experimental measurements, given the ferrimagnetic nature of the RE-TM magnets [38]. Already, the current calculations have found the high-temperature RE magnetic

ordering to be strongest in SmCo$_5$, the best-performing magnet in the RECo$_5$ family.

APPENDIX A: COUPLING INTRODUCED BY THE LSIC

Here, we list the formulas for the different coupling functions which enter the coupled equations (13). Again, we emphasize that $\kappa = -l - 1$ and $\kappa' = l$. We have also introduced the quantities $\bar{l}_1 = l + 1$ and $\bar{l}_2 = l - 1$:

$$\mathcal{G}_\pm^{m_j}(\kappa,\kappa) = \frac{2m_j}{2l+1}B_{XC} \pm \left[V_{l(m_j-1/2)}^\uparrow \left(\frac{l+m_j+1/2}{2l+1} \right) + V_{l(m_j+1/2)}^\downarrow \left(\frac{l-m_j+1/2}{2l+1} \right) \right],$$

$$\mathcal{G}_\pm^{m_j}(\kappa',\kappa') = -\frac{2m_j}{2l+1}B_{XC} \pm \left[V_{l(m_j-1/2)}^\uparrow \left(\frac{l-m_j+1/2}{2l+1} \right) + V_{l(m_j+1/2)}^\downarrow \left(\frac{l+m_j+1/2}{2l+1} \right) \right],$$

$$\mathcal{G}_\pm^{m_j}(\kappa,\kappa') = -\left(1 - \frac{m_j^2}{(l+1/2)^2} \right)^{\frac{1}{2}} \left[B_{XC} \mp \frac{V_{l(m_j-1/2)}^\uparrow - V_{l(m_j+1/2)}^\downarrow}{2} \right] = \mathcal{G}_\pm^{m_j}(\kappa',\kappa),$$

$$\mathcal{G}_\pm^{m_j}(-\kappa,-\kappa) = -\frac{2m_j}{2\bar{l}_1+1}B_{XC} \pm \left[V_{\bar{l}_1(m_j-1/2)}^\uparrow \left(\frac{\bar{l}_1-m_j+1/2}{2\bar{l}_1+1} \right) + V_{\bar{l}_1(m_j+1/2)}^\downarrow \left(\frac{\bar{l}_1+m_j+1/2}{2\bar{l}_1+1} \right) \right],$$

$$\mathcal{G}_\pm^{m_j}(-\kappa',-\kappa') = -\frac{2m_j}{2\bar{l}_2+1}B_{XC} \pm \left[V_{\bar{l}_2(m_j-1/2)}^\uparrow \left(\frac{\bar{l}_2-m_j+1/2}{2\bar{l}_2+1} \right) + V_{\bar{l}_2(m_j+1/2)}^\downarrow \left(\frac{\bar{l}_2+m_j+1/2}{2\bar{l}_2+1} \right) \right].$$
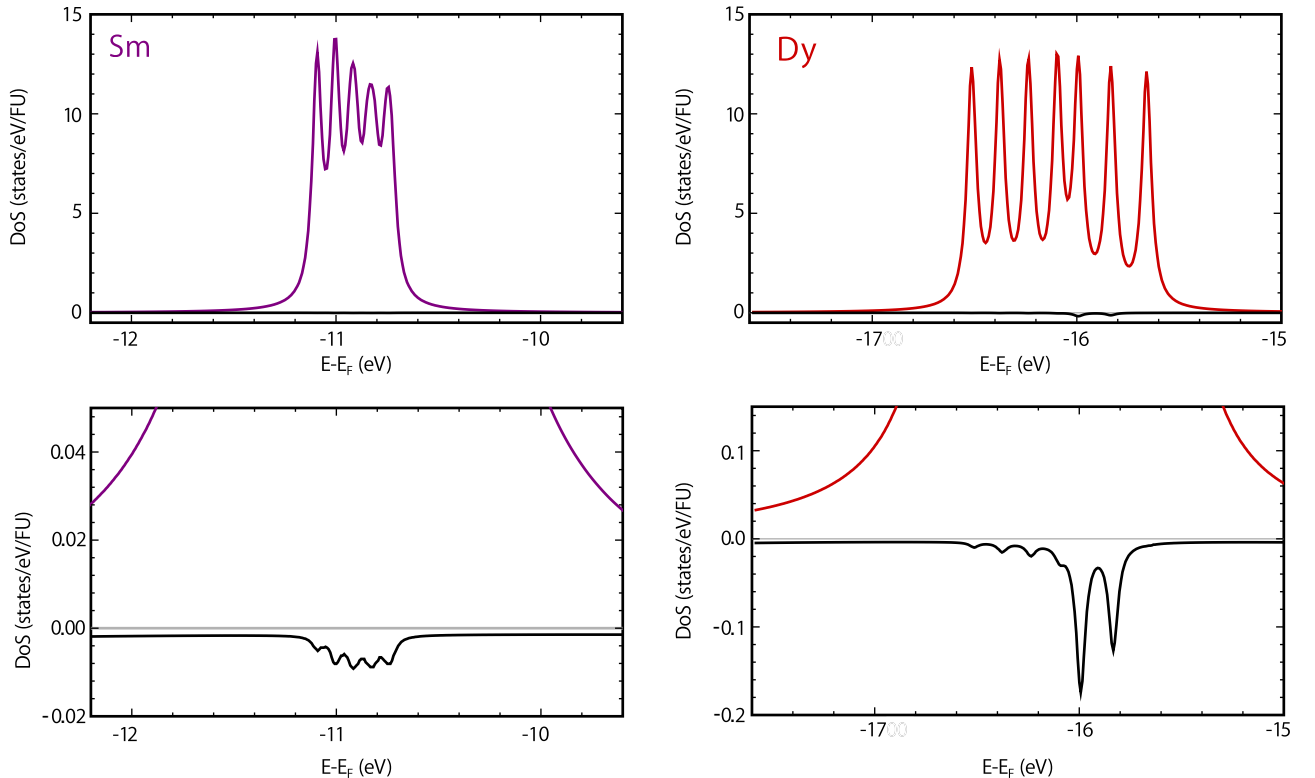

FIG. 10. Spin-resolved, zero-temperature DOS for SmCo$_5$ (left) and DyCo$_5$ (right), at energies corresponding to the majority-spin, SI-corrected states. The majority- and minority-spin contributions are plotted with positive and negative signs, respectively, and the lower plots zoom in on the minority contribution. Note the larger scale for DyCo$_5$.

APPENDIX B: RELATIVISTIC COUPLINGS BETWEEN DIFFERENT SPIN-ORBITAL CHANNELS

As indicated by Eq. (15), the spin-orbit interaction mixes different (σ, m) channels, including those which do and do not have the LSIC applied. In general, since there is a large energy separation between corrected and uncorrected states (~ 10 eV), the energy denominator that appears in the perturbative expansion of the state is large and thus the mixing is small. Nonetheless, the mixing can be seen by examining the zero-temperature, spin-resolved DOS at energies around the occupied (majority spin) $4f$ electrons.

This quantity is plotted in Fig. 10 for $SmCo_5$ and $DyCo_5$. In the scalar-relativistic calculation, the occupied $4f$ electrons are spin pure, but on performing the relativistic calculation a small contribution appears in the minority-spin channel (negative scale in Fig. 10), due to the mixing described above. This contribution is bigger for $DyCo_5$ than $SmCo_5$ (note change of scale) because there are two SI-corrected minority-spin states located 4 eV above the majority-spin peak which mix more strongly. For $SmCo_5$, the mixing only occurs with SI-uncorrected states lying above the Fermi level. The large energy separation suppresses the mixing in this case.
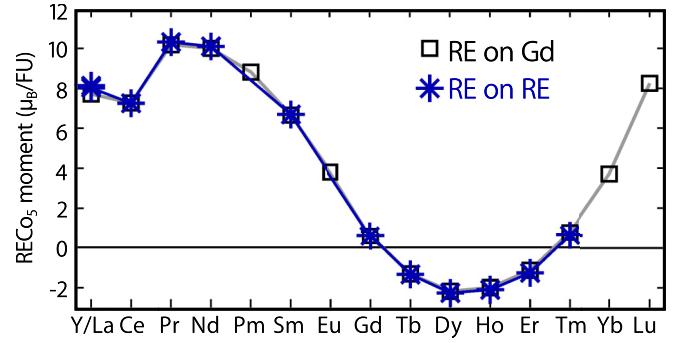

FIG. 11. Magnetic moments calculated at zero temperature for $RECo_5$ using $GdCo_5$ lattice parameters (squares), and $RECo_5$ using $RECo_5$ lattice parameters (stars).

APPENDIX C: ZERO-TEMPERATURE MOMENTS CALCULATED AT EXPERIMENTAL LATTICE PARAMETERS

In Fig. 11, we compare the zero-temperature moments calculated either using $GdCo_5$ lattice parameters or, where available, $RECo_5$ lattice parameters (Table I). Note that these calculations were performed without the OPC applied, which results in reduced Co moments compared to Fig. 3.

[1] R. J. Elliott, in *Magnetic Properties of Rare Earth Metals*, edited by R. J. Elliott (Plenum, London, 1972), p. 1.

[2] D. C. Koskenmaki and K. A. Gschneidner, Jr., in *Handbook on the Physics and Chemistry of Rare Earths*, edited by K. A. Gschneidner, Jr. and L. Eyring (North-Holland, Amsterdam, 1978), p. 337.

[3] V. Zepf, Rare earth elements: What and where they are, in *Rare Earth Elements: A New Approach to the Nexus of Supply, Demand and Use: Exemplified along the Use of Neodymium in Permanent Magnets* (Springer, Berlin, 2013), pp. 11–39.

[4] K. Strnat, G. Hoffer, J. Olson, W. Ostertag, and J. J. Becker, J. Appl. Phys. **38**, 1001 (1967).

[5] M. Sagawa, S. Fujimura, N. Togawa, H. Yamamoto, and Y. Matsuura, J. Appl. Phys. **55**, 2083 (1984).

[6] J. J. Croat, J. F. Herbst, R. W. Lee, and F. E. Pinkerton, J. Appl. Phys. **55**, 2078 (1984).

[7] O. Gutfleisch, M. A. Willard, E. Brück, C. H. Chen, S. G. Sankar, and J. P. Liu, Adv. Mater. **23**, 821 (2011).

[8] J. M. D. Coey, IEEE Trans. Magn. **47**, 4671 (2011).

[9] M. D. Kuz'min and A. M. Tishin, in *Handbook of Magnetic Materials*, edited by K. H. J. Buschow (Elsevier, Amsterdam, 2008), Vol. 17, Chap. 3, p. 149.

[10] K. H. J. Buschow, Rep. Prog. Phys. **40**, 1179 (1977).

[11] S. Chikazumi, *Physics of Ferromagnetism*, 2nd ed. (Oxford University Press, Oxford, 1997), p. 62.

[12] Z. Tie-song, J. Han-min, G. Guang-hua, H. Xiu-feng, and C. Hong, Phys. Rev. B **43**, 8593 (1991).

[13] A. V. Andreev, in *Handbook of Magnetic Materials*, edited by K. H. J. Buschow (North-Holland, New York, 1995), Vol. 8, Chap. 2, p. 59.

[14] W. Kohn and L. J. Sham, Phys. Rev. **140**, A1133 (1965).

[15] B. L. Györffy, A. J. Pindor, J. Staunton, G. M. Stocks, and H. Winter, J. Phys. F: Met. Phys. **15**, 1337 (1985).

[16] J. B. Staunton, L. Szunyogh, A. Buruzs, B. L. Györffy, S. Ostanin, and L. Udvardi, Phys. Rev. B **74**, 144411 (2006).

[17] M. Lüders, A. Ernst, M. Däne, Z. Szotek, A. Svane, D. Ködderitzsch, W. Hergert, B. L. Györffy, and W. M. Temmerman, Phys. Rev. B **71**, 205109 (2005).

[18] E. Mendive-Tapia and J. B. Staunton, Phys. Rev. Lett. **118**, 197202 (2017).

[19] C. E. Patrick, S. Kumar, G. Balakrishnan, R. S. Edwards, M. R. Lees, E. Mendive-Tapia, L. Petit, and J. B. Staunton, Phys. Rev. Mater. **1**, 024411 (2017).

[20] L. Petit, D. Paudyal, Y. Mudryk, K. A. Gschneidner, V. K. Pecharsky, M. Lüders, Z. Szotek, R. Banerjee, and J. B. Staunton, Phys. Rev. Lett. **115**, 207201 (2015).

[21] I. D. Hughes, M. Däne, A. Ernst, W. Hergert, M. Lüders, J. Poulter, J. B. Staunton, A. Svane, Z. Szotek, and W. M. Temmerman, Nature (London) **446**, 650 (2007).

[22] S. Baroni, S. de Gironcoli, A. Dal Corso, and P. Giannozzi, Rev. Mod. Phys. **73**, 515 (2001).

[23] F. Giustino, Rev. Mod. Phys. **89**, 015003 (2017).

[24] J. B. Staunton, Rep. Prog. Phys. **57**, 1289 (1994).

[25] A. J. Cohen, P. Mori-Sánchez, and W. Yang, Science **321**, 792 (2008).

[26] F. Illas, I. de P. R. Moreira, J. M. Bofill, and M. Filatov, Phys. Rev. B **70**, 132414 (2004).

[27] A. Liechtenstein, M. Katsnelson, V. Antropov, and V. Gubanov, J. Magn. Magn. Mater. **67**, 65 (1987).

[28] K. Cao, G.-C. Guo, D. Vanderbilt, and L. He, Phys. Rev. Lett. **103**, 257201 (2009).

[29] N. M. Rosengaard and B. Johansson, Phys. Rev. B **55**, 14975 (1997).

[30] A. Kashyap, R. Skomski, R. F. Sabiryanov, S. S. Jaswal, and D. J. Sellmyer, IEEE Trans. Magn. **39**, 2908 (2003).

[31] I. Turek, J. Kudrnovský, G. Bihlmayer, and S. Blügel, J. Phys.: Condens. Matter **15**, 2771 (2003).

[32] F. Körmann, A. Dick, T. Hickel, and J. Neugebauer, Phys. Rev. B **79**, 184406 (2009).

[33] T. Fukazawa, H. Akai, Y. Harashima, and T. Miyake, J. Appl. Phys. **122**, 053901 (2017).

[34] F. Körmann, B. Grabowski, B. Dutta, T. Hickel, L. Mauger, B. Fultz, and J. Neugebauer, Phys. Rev. Lett. **113**, 165503 (2014).

[35] B. L. Györffy and G. M. Stocks, in *Electrons in Disordered Metals and at Metallic Surfaces*, edited by P. Phariseau and B. Györffy (Springer, New York, 1979), Chap. 4, pp. 89–192.

[36] H. Ebert, D. Ködderitzsch, and J. Minár, Rep. Prog. Phys. **74**, 096501 (2011).

[37] J. B. Staunton, S. Ostanin, S. S. A. Razee, B. L. Györffy, L. Szunyogh, B. Ginatempo, and E. Bruno, Phys. Rev. Lett. **93**, 257204 (2004).

[38] C. E. Patrick, S. Kumar, G. Balakrishnan, R. S. Edwards, M. R. Lees, L. Petit, and J. B. Staunton, Phys. Rev. Lett. **120**, 097202 (2018).

[39] M. Matsumoto, R. Banerjee, and J. B. Staunton, Phys. Rev. B **90**, 054421 (2014).

[40] E. Bruno and B. Ginatempo, Phys. Rev. B **55**, 12946 (1997).

[41] O. K. Andersen, A. V. Postnikov, and S. Y. Savrasov, Mater. Res. Soc. Symp. Proc. **253** (1991).

[42] A. Deák, E. Simon, L. Balogh, L. Szunyogh, M. dos Santos Dias, and J. B. Staunton, Phys. Rev. B **89**, 224401 (2014).

[43] S. H. Vosko, L. Wilk, and M. Nusair, Can. J. Phys. **58**, 1200 (1980).

[44] J. P. Perdew and A. Zunger, Phys. Rev. B **23**, 5048 (1981).

[45] O. Eriksson, B. Johansson, R. C. Albers, A. M. Boring, and M. S. S. Brooks, Phys. Rev. B **42**, 2707 (1990).

[46] G. Kotliar, S. Y. Savrasov, K. Haule, V. S. Oudovenko, O. Parcollet, and C. A. Marianetti, Rev. Mod. Phys. **78**, 865 (2006).

[47] A. I. Lichtenstein and M. I. Katsnelson, Phys. Rev. B **57**, 6884 (1998).

[48] I. L. M. Locht, Y. O. Kvashnin, D. C. M. Rodrigues, M. Pereiro, A. Bergman, L. Bergqvist, A. I. Lichtenstein, M. I. Katsnelson, A. Delin, A. B. Klautau, B. Johansson, I. Di Marco, and O. Eriksson, Phys. Rev. B **94**, 085137 (2016).

[49] O. Grånäs, I. D. Marco, P. Thunström, L. Nordström, O. Eriksson, T. Björkman, and J. Wills, Comput. Mater. Sci. **55**, 295 (2012).

[50] P. Söderlind, A. Landa, I. L. M. Locht, D. Åberg, Y. Kvashnin, M. Pereiro, M. Däne, P. E. A. Turchi, V. P. Antropov, and O. Eriksson, Phys. Rev. B **96**, 100404 (2017).

[51] P. Delange, S. Biermann, T. Miyake, and L. Pourovskii, Phys. Rev. B **96**, 155132 (2017).

[52] M. S. S. Brooks, L. Nordstrom, and B. Johansson, J. Phys.: Condens. Matter **3**, 2357 (1991).

[53] M. Richter and H. Eschrig, Phys. B (Amsterdam) **172**, 85 (1991).

[54] L. Steinbeck, M. Richter, and H. Eschrig, Phys. Rev. B **63**, 184431 (2001).

[55] P. Larson, I. I. Mazin, and D. A. Papaconstantopoulos, Phys. Rev. B **69**, 134408 (2004).

[56] P. Larson, I. I. Mazin, and D. A. Papaconstantopoulos, Phys. Rev. B **67**, 214405 (2003).

[57] O. Waller, P. Piekarz, A. Bosak, P. T. Jochym, S. Ibrahimkutty, A. Seiler, M. Krisch, T. Baumbach, K. Parlinski, and S. Stankov, Phys. Rev. B **94**, 014303 (2016).

[58] P. Söderlind, P. E. A. Turchi, A. Landa, and V. Lordi, J. Phys.: Condens. Matter **26**, 416001 (2014).

[59] S. Lebègue, G. Santi, A. Svane, O. Bengone, M. I. Katsnelson, A. I. Lichtenstein, and O. Eriksson, Phys. Rev. B **72**, 245102 (2005).

[60] M. Cococcioni and S. de Gironcoli, Phys. Rev. B **71**, 035105 (2005).

[61] K. Karlsson, F. Aryasetiawan, and O. Jepsen, Phys. Rev. B **81**, 245113 (2010).

[62] P. Strange, *Relativistic Quantum Mechanics* (Cambridge University Press, Cambridge, 1998).

[63] P. Strange, J. Staunton, and B. L. Györffy, J. Phys. C: Solid State Phys. **17**, 3355 (1984).

[64] H. Ebert, Fully relativistic band structure calculations for magnetic solids: Formalism and application, in *Electronic Structure and Physical Properies of Solids: The Uses of the LMTO Method Lectures of a Workshop Held at Mont Saint Odile, France, October 2–5,1998*, edited by H. Dreyssé (Springer, Berlin, 2000), pp. 191–246.

[65] M. Däne, M. Lüders, A. Ernst, D. Ködderitzsch, W. M. Temmerman, Z. Szotek, and W. Hergert, J. Phys.: Condens. Matter **21**, 045604 (2009).

[66] W. B. Jensen, Found. Chem. **17**, 23 (2015).

[67] P. Strange, A. Svane, W. M. Temmerman, Z. Szotek, and H. Winter, Nature (London) **399**, 756 (1999).

[68] L. Nordström, O. Eriksson, M. S. S. Brooks, and B. Johansson, Phys. Rev. B **41**, 9111 (1990).

[69] M. S. S. Brooks, O. Eriksson, and B. Johansson, J. Phys.: Condens. Matter **1**, 5861 (1989).

[70] E. A. Nesbitt, H. J. Williams, J. H. Wernick, and R. C. Sherwood, J. Appl. Phys. **33**, 1674 (1962).

[71] M. Richter, J. Phys. D: Appl. Phys. **31**, 1017 (1998).

[72] K. Kumar, J. Appl. Phys. **63**, R13 (1988).

[73] H. Kohlmann, T. C. Hansen, and V. Nassif, Inorg. Chem. **57**, 1702 (2018).

[74] K. N. R. Taylor and I. M. Darby, in *Physics of Rare Earth Solids* (Chapman and Hall, London, 1972), p. 60.

[75] K. Hummler and M. Fähnle, Phys. Rev. B **53**, 3272 (1996).